Implementation of Information Entropy, *b*-Value, and Regression Analyses for Temporal Evaluation of Acoustic Emission Data Recorded during ASR Cracking

V. Soltangharaei, M.ASCE[1]; L. Ai[2]; R. Anay[3]; M. Bayat, M.ASCE[4]; and P. Ziehl, M.ASCE[5]

Abstract: This study investigates the efficacy of differing information entropy calculation approaches for concrete structures undergoing alkali-silica reaction (ASR)-induced cracking. In prior work, information entropy has only been utilized for a better understanding of the damage in metallic structures under external loading. To our knowledge, no research has been published regarding information entropy for concrete structures affected by ASR. This scientific gap is addressed in this paper. Furthermore, the innovation lies in using coefficients of determination instead of *b*-values for cracking identification. The entropy results show that the randomness of events increases at the earlier stage of ASR, which is expected due to the microcrack formation, and decreases at the later stage due to the formation of macrocracks. Moreover, a correlation is observed between the coefficients of determination and the evolution of the cumulative signal strength.
DOI: 10.1061/(ASCE)SC.1943-5576.0000550.

Author keywords: Acoustic emission (AE); Alkali-silica reaction (ASR); *b*-value analysis; Damage evaluation; Information entropy.

Introduction

One potential source of degradation in concrete structures is the alkali-silica reaction (ASR) (Bach et al. 1993; Clark 1989). This chemical reaction occurs between siliceous minerals in some aggregates and alkali hydroxides in pore solutions (Barbosa et al. 2018; Rajabipour et al. 2015). The chemical product is a hygroscopic material called alkali-silica gel, which absorbs water causing its volume to increase. The rise in the volume of gel induces stress to aggregates, and the cement matrix causes cracking and damage (Garcia-Diaz et al. 2006; Saouma and Hariri-Ardebili 2014). The cracking in cementitious material leads to strength reduction and damage in the material. The chemical reaction gradually continues for several years (Fernandes and Broekmans 2013). In a laboratory, aging caused by ASR is usually accelerated by exposing concrete specimens to high temperatures and humidity exceeding 80% (Garcia-Diaz et al. 2006).

Several methods have been employed to detect ASR and the corresponding damage in concrete structures, including visual inspection, petrographic analysis, demountable mechanical strain gauges (DEMEC gauge), and a cracking index (Islam and Ghafoori 2018; Allard et al. 2018; Sinno and Shehata 2019; Hayes et al. 2018; Thomas et al. 2013; Fournier et al. 2010). These methods are not always efficient in early damage detection. The ASR cracking initiates inside structures and sometimes appears very late on the surface of the concrete. Therefore, visual inspection is not a reliable method for the early detection of ASR cracking. The DEMEC gauge and cracking index are usually used on the surface of the concrete to measure the expansion and crack width. In some structures, like shear walls, the expansion mostly occurs out-of-plane rather than in-plane due to the in-plane stress restraint. Therefore, the expansion and resulting cracking do not appear on the surface until the end of the reaction, and the DEMEC gauge and cracking index are not useful for the ASR detection. In addition, some methods (e.g., coring and petrographic analysis enabled through coring) are destructive and sometimes prohibited in sensitive structures, such as nuclear structures and prestressed concrete elements.

Nondestructive structural health monitoring systems may be alternatives to compensate for the drawbacks attributed to the traditional methods. Acoustic emission (AE) can fall under this category and is a passive system, which can be employed to monitor structures continuously. AE piezometric sensors are sensitive to cracking initiation and growth and can be attached to one side of structures. The sensors detect and record elastic stress waves emitted due to crack formation. In addition, source localization is feasible with an appropriate sensor layout. Recently, research has been conducted to employ AE for monitoring ASR-induced damage (Abdelrahman et al. 2015; Farnam et al. 2015; Lokajíček et al. 2017) using signal features such as cumulative signal strength and amplitude (parametric features). Although correlations between some parametric AE features, such as cumulative signal strength (CSS) and ASR expansion, have been observed in the literature, the parametric features may not be appropriate options to assess the condition of structures and make a comparison between data collected from different structures due to the high-dependency of them on sources to sensor distance, structure dimensions, sensor type, and concrete material. Therefore, one of the scientific gaps in

[1]Postdoctoral Fellow, Dept. of Civil and Environmental Engineering, Univ. of South Carolina, Columbia, SC 29208. Email: vafa@email.sc.edu

[2]Graduate Research Assistant, Dept. of Civil and Environmental Engineering, Univ. of South Carolina, Columbia, SC 29208. ORCID: https://orcid.org/0000-0003-2938-5533. Email: ail@email.sc.edu

[3]Postdoctoral Researcher, Dept. of Civil and Environmental Engineering, Univ. of South Carolina, Columbia, SC 29208; Lecturer, Dept. of Building and Construction Engineering Technology, Northern Technical Univ., Nineveh, Iraq. Email: ranay@email.sc.edu

[4]Research Associate Professor, Dept. of Civil and Environmental Engineering, Univ. of South Carolina, Columbia, SC 29208 (corresponding author). ORCID: https://orcid.org/0000-0002-0990-7077. Email: mbayat@mailbox.sc.edu; mbayat14@yahoo.com

[5]Professor, Dept. of Civil and Environmental Engineering, Univ. of South Carolina, Columbia, SC 29208. Email: ziehl@cec.sc.edu

Note. This manuscript was submitted on May 26, 2020; approved on September 9, 2020; published online on December 3, 2020. Discussion period open until May 3, 2021; separate discussions must be submitted for individual papers. This paper is part of the ***Practice Periodical on Structural Design and Construction***, © ASCE, ISSN 1084-0680.

this field is finding potential alternatives to address the problem with the parametric features. In this paper, Shannon entropy has been utilized to address some deficiencies related to the parametric features.

Shannon entropy (information entropy) has recently been investigated for the damage evaluation of metallic material under fatigue loading (Chai et al. 2018; Kahirdeh et al. 2017a; Unnthorsson et al. 2008; Amiri et al. 2015; Amiri and Modarres 2014; Kahirdeh and Khonsari 2016; Zhang et al. 2015). Kahirdeh et al. (2017a) utilized information entropy and relative entropy to study the damage evolution of bone-shaped aluminum specimens under cyclic loading. The trend of standardized cumulative entropy was similar to the Vickers hardness trend. Chai et al. (2018) calculated a Shannon entropy for hits recorded during a fatigue crack growth test conducted on a notched alloyed steel plate and a monotonic three-point bending test conducted on a small stainless-steel beam. The results indicated that Shannon entropies for AE signals were useful to inform discrimination between damage stages, while the temporal distribution of amplitude did not show any clear trend.

Although some studies have been conducted regarding an application of information entropy as a damage criterion for metallic material under cyclic loading, to our knowledge, research has not been published regarding information entropy for cementitious materials under different loading conditions or the ASR process. Therefore, in this study, information entropy results for the damage evaluation of cementitious material with different scales and under different stress boundary conditions are presented to evaluate the efficacy of the method for the condition assessment of concrete structures affected by ASR. To evaluate the effect of the specimen size on the values of Shannon entropy, two sets of concrete specimens (medium-scale and large-scale), which were exposed to ASR expansion, were utilized in addition to a small-scale cement prism under compressive loading.

Several AE-based analyses, such as intensity and *b*-value analyses, have been proposed and employed in the previous literature to evaluate damage in structures under external loading (Noorsuhada 2016; Rao and Lakshmi 2005; Colombo et al. 2003; Jung et al. 2017; Lamonaca et al. 2014; Abdelrahman et al. 2014; Sagasta et al. 2018; Nair and Cai 2010). Despite a large amount of literature regarding the application of the AE analyses for structures under loading (Noorsuhada 2016; Rao and Lakshmi 2005; Colombo et al. 2003; Jung et al. 2017; Lamonaca et al. 2014; Abdelrahman et al. 2014; Nair and Cai 2010), limited research has been published about using these analyses for the damage evaluation of structures under ASR-induced stresses (Abdelrahman et al. 2015). Therefore, in this study, a *b*-value analysis and a method based on the coefficients of determination and linear regression analysis are also used to evaluate the temporal evolution of AE data for the medium-size specimens during the ASR process.

Test Setup

In this study, AE data for three types of specimens having different scales were investigated to study the effect of the combination of variables, such as dimension, sensor sensitivity, and loading, on Shannon entropy values. Each specimen type has a different test setup and boundary conditions. The medium-scale specimens were concrete blocks with dimensions of $305 \times 305 \times 1{,}120$ mm with differing reinforcement conditions. Two specimens possessed reactive coarse aggregates (reactive specimens). One of the reactive specimens had steel reinforcement along two dimensions (length and depth), which is referred to as the medium-scale confined specimen in this paper. The other reactive specimen did not have

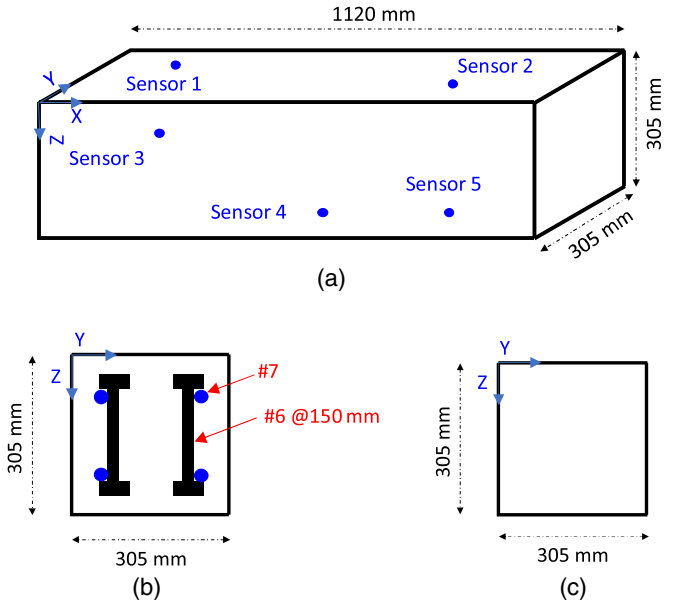

Fig. 1. Dimension and sensor layout of medium-scale specimens: (a) medium-scale specimens; (b) specimen section for the confined specimen; and (c) specimen section for the unconfined specimen.

any steel reinforcement and is referred to as the medium-scale unconfined specimen. The detail of the medium-scale specimen is shown in Fig. 1. The specimens were kept in a chamber with high humidity and temperature (95% ± 5% and 37°C ± 3°C) to accelerate the aging process. Ten broadband AE sensors were mounted on the surfaces of the reactive specimens. The sensors were PKWDI (MISTRAS Group, Princeton Junction, New Jersey) with the frequency operating range of 200–850 kHz and 26-dB internal preamplifications. A 24-channel Micro-II Express, manufactured by MISTRAS Group, was utilized as a data acquisition system. The sampling rate was 5,000 kHz, the pretrigger time was 256 μs, and the hit definition time (HDT), peak definition time (PDT), and hit lockout time (HLT) were 400, 200, and 200 μs, respectively. The AE data acquisition starts to record a hit when the voltage exceeds the threshold of the system. The HDT is a time that is defined in the AE system for ending hits. The hit recording is stopped when an amount of time equal to the HDT has elapsed without any threshold crossings. The HDT is a time parameter, which is defined in the AE system to remove tailing in hits caused by wave reflections. This parameter is defined at the end of the signal, where any threshold crossing during that time is ignored. The PDT is the time that is defined in the system to find the peak and rise time in signals. Bandpass digital and analog filters with a frequency range of 20–400 kHz were set in the data acquisition system. A background test was conducted before the test, and the threshold was set at 32 dB. More details about the medium-scale specimens can be found in the study by Soltangharaei et al. (2020).

Also included in the study are two large-scale concrete specimens with dimensions of $3{,}500 \times 3{,}000 \times 1{,}000$ mm. The two specimens have reactive aggregates. The specimens had reinforcement on the top and bottom of the specimens. One of the specimens was restrained in a rigid steel frame, which is referred to as the large-scale confined specimen. The other specimen was not enclosed by a steel frame, namely, the large-scale unconfined specimen in this study. The test setup details are explained in Soltangharaei et al. (2018a). In this study, the AE data for the reactive specimens is investigated. The specimens were kept in a large chamber with high

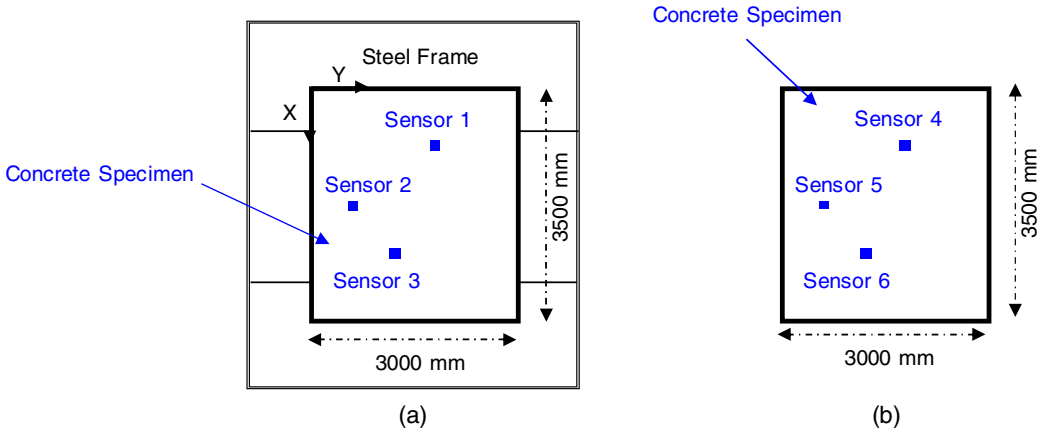

Fig. 2. Dimension and sensor layout of large-scale specimens: (a) confined; and (b) unconfined.

humidity and temperature similar to the medium-scale specimens. Three broadband AE sensors were embedded in the specimens before casting. The sensors were WDIUC-AST (manufactured by MISTRAS Group) with the operating frequency range of 200–900 kHz and internal low-noise 40 dB preamplifiers. A 16-channel Sensor Highway II (SHII), manufactured by MISTRAS Group, was utilized as the data acquisition system. The sampling rate was set to 1,000 kHz, the pretrigger time was 256 μs, and the HDT, HLT, and PDT were 400, 200, and 200 μs, respectively. The initial data acquisition threshold was 32 dB. The schematic figure for the large-scale specimens is illustrated in Fig. 2.

The third specimen investigated in this study is a relatively small cement paste specimen (referred to as the small-scale specimen) with dimensions of $38.1 \times 38.1 \times 152.4$ mm loaded in uniaxial compression. Eight micro-30 resonant sensors (with an operating frequency range of 150–400 kHz and external preamplifiers with 40 dB gain) were attached to the specimen surfaces close to the specimen's ends because the cracking started at the ends in the cement-paste. A sufficient amount of data was collected using the eight sensors. In addition, this number of sensors had a minimal effect on the cracking mechanism in the cement paste. A 16-channel DiSP system manufactured by MISTRAS Group, was utilized for the data acquisition. Preamplifiers with a 40 dB gain and bandpass internal filters with the frequency range of 100–1,200 kHz were connected to the sensors. The sampling rate was set to 1,000 kHz, the pretrigger time was 256 μs, and the HDT, HLT, and PDT were 400, 200, and 200 μs. The initial data acquisition threshold was 32 dB. The small-scale specimen is shown in Fig. 3.

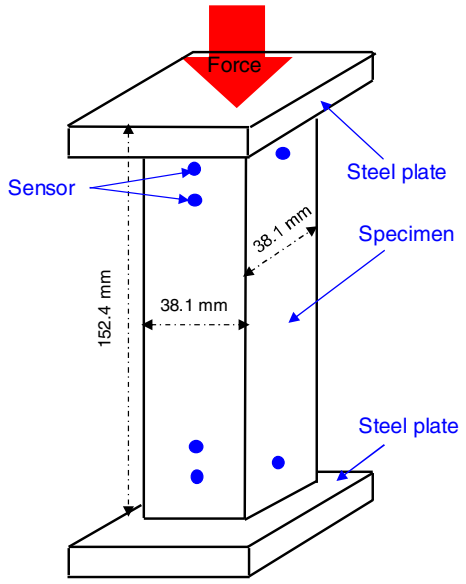

Fig. 3. Dimension and sensor layout of small-scale specimens.

Analysis Method and Procedure

AE data were utilized to calculate signal entropies in all three specimen types. Conventional features, such as amplitude and signal strength, were used in addition to entropies to evaluate the temporal trend of data. Methods for calculating signal entropies and damage indices are presented in the following subsections.

Signal Entropy

Two methods for calculating signal entropy may be found in the literature, and they have been employed for fatigue loading (Chai et al. 2018; Kahirdeh et al. 2017b; Kahirdeh 2014; Sauerbrunn 2016; Kahirdeh and Khonsari 2016). The methods, which include voltage amplitude entropy and feature entropy, are presented in this section.

Voltage entropy is calculated based on the distribution of amplitude voltages of AE signals. The voltage amplitudes of each AE signal are used to develop a histogram of the signal. The bin size is recommended to be close to the resolution of the AE data acquisition systems (Chai et al. 2018). The resulting histogram contains several bars corresponding to the bins. Each bar shows the relative frequency of voltages within a bin. The frequency of voltages within a bin is the number of signal samples, and their voltages are within the bin range. The relative frequency is calculated by dividing the frequency of voltages by the total number of signal samples. Then, the voltage entropy is calculated according to the Shannon entropy equation

$$\text{Entropy} = -\sum_{i=1}^{n} P(x_i) \times \log(P(x_i)) \tag{1}$$

where n = number of bins in each signal; x_i = bins defined in each signal; and $P(x_i)$ = relative frequency of each bin calculated according to the signal histogram. The procedure is shown in Fig. 4. With this method, it is assumed that the voltage value changes constantly and independently between the samples. There are two

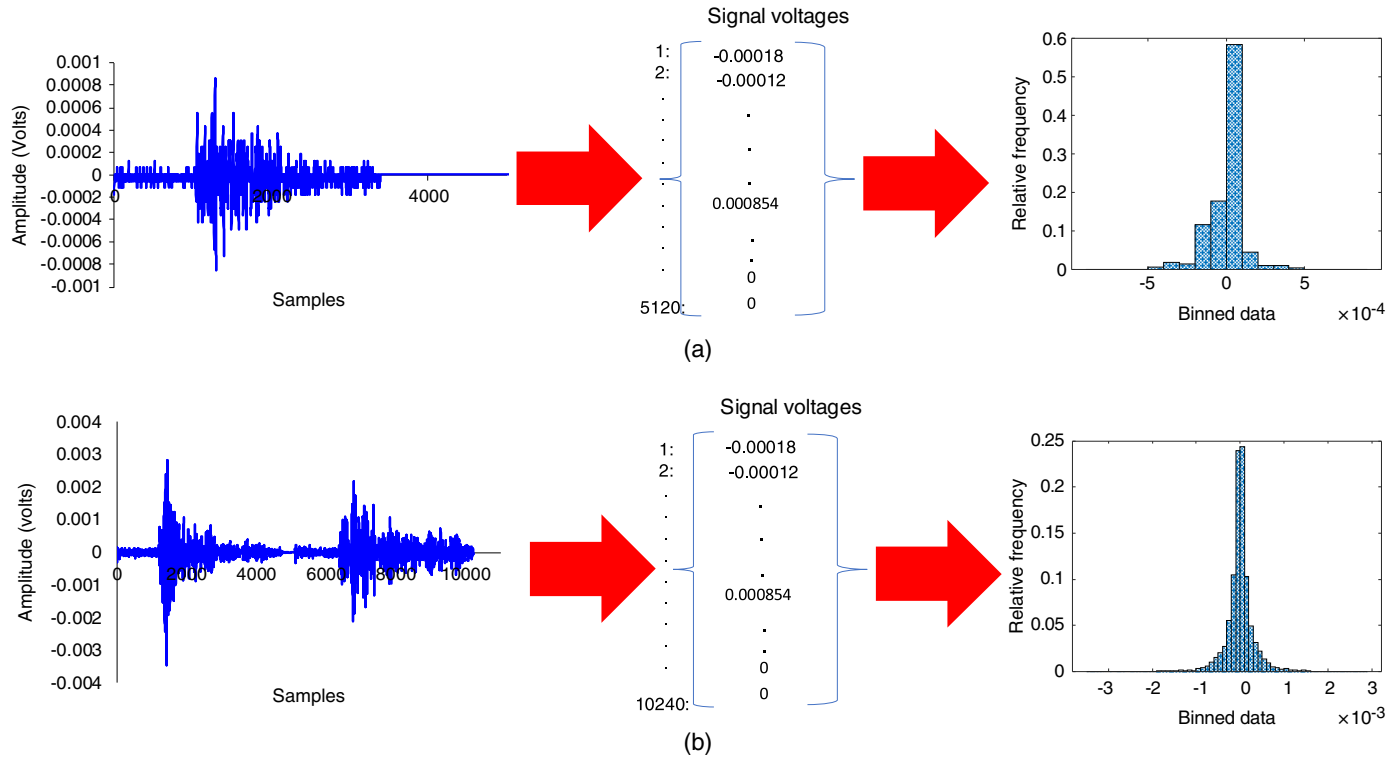

Fig. 4. Entropy calculation using signal amplitude voltage: (a) discrete voltage entropy; and (b) global voltage entropy.

approaches to calculate entropy. One approach is to calculate the entropy for each signal, namely, the discrete voltage entropy (DVE) in this paper [Fig. 4(a)]. The other approach is to calculate the entropy based on all signal voltages up to the desired experiment time. In this method, the amplitude voltages of all signals up to the desired time are used to derive a histogram and calculate an entropy. This method is referred to as the global voltage entropy (GVE). In Fig. 4(b), the signal voltages for two signals were used for developing a histogram and calculating the associated entropy. The next entropy is calculated by using three signals. This is continued until all signals are included in the calculation.

Another method is referred to as counts-entropy. There are two methods for calculating counts-entropy. For both calculation methods, it is assumed that each count is independent of other counts. In the first calculation method, the probability is calculated by dividing the counts of a signal corresponding to the desired time over the cumulative counts up to that time. Then the counts-entropy is calculated by using the Shannon entropy Eq. (1). This method is referred to as CE. CE will be updated when a new signal is received. In the second procedure, the cumulative distribution function (CDF) for counts up to the desired time is estimated by using the empirical CDF method (Kahirdeh 2014), and the corresponding probability distribution function (PDF) is derived. The entropy is estimated using the probability distribution for each bin using Eq. (1). This method is referred to as CE_CDF in this study. The procedure is repeated when a new signal is received.

AE Damage Index Methods

One common method for damage (cracking) detection using AE is the b-value analysis. This method is based on the Gutenberg-Ritcher equation in seismology (Colombo et al. 2003). The modified version of the equation has been utilized in AE for damage identification (Rao and Lakshmi 2005; Colombo et al. 2003; Jung et al. 2017). An almost-linear distribution between the logarithm of AE amplitude-frequency and AE amplitude is derived for a data set, and the slope of a fitted line to the distribution is referred to as the b-value. A smaller absolute b-value shows the contribution of AE data with higher amplitudes and is expected to be related to the damage formation. The b-values are usually calculated using the following equation:

$$\log N = a - b\left(\frac{A_{dB}}{20}\right) \tag{2}$$

where N = number of AE hits with a magnitude equal to or greater than an amplitude of a hit. The linear regression is conducted between the $\log N$ and $A_{dB}/20$ to calculate the model parameters (a and b). All data are separated into a specific subset number. Then, the b-values are calculated separately in each subset. This method is referred to as the incremental b-value (Inc-b).

The coefficient of determination (R^2) for each b-value is calculated. The coefficients may also be considered as a damage identification criterion because it is expected that severe damage formation emits AE signals with large amplitudes. The AE signals with large amplitudes cause a deviation from the mostly linear amplitude-$\log N$ distribution and, consequently, a reduction in the coefficients of determination. The R^2 is calculated for each subset of AE data according to the following formulation:

$$R^2 = 1 - \frac{\sum_{i=1}^{n}(\hat{y}_i - y_i)^2}{\sum_{i=1}^{n}(y_i - \bar{y})^2} \tag{3}$$

where $\hat{y}_i$ = estimated value of $\log N$ for an ith point by using the fitted line; y_i = real value of $\log N$ for the ith point; and $\bar{y}$ = average value of $\log N$. The index n denotes the last desired data to calculate the b-value.

Pract. Period. Struct. Des. Constr., 2021, 26(1): 04020065

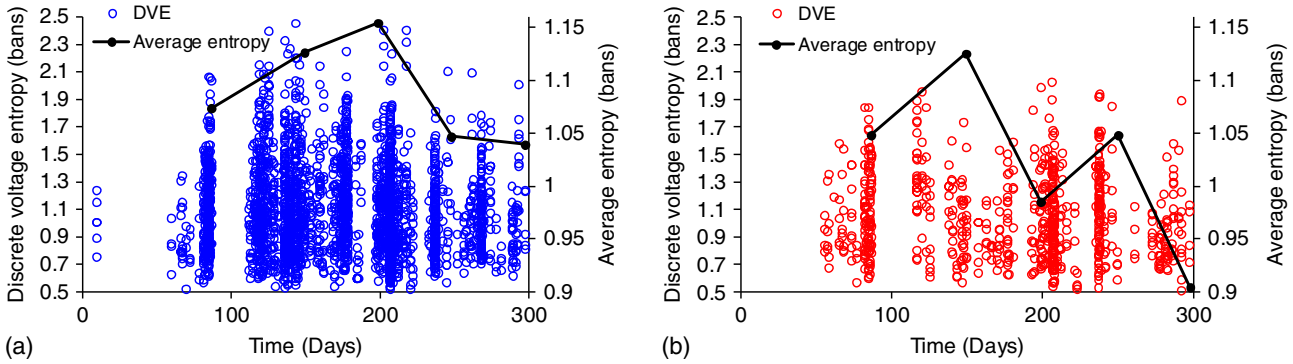

Fig. 5. Discrete voltage entropy (DVE) for medium-scale specimens, with a bin size of 0.0001 V: (a) confined specimen; and (b) unconfined specimen.

The log N versus amplitude distribution is usually not perfectly linear, especially for large and small amplitudes (upper and lower part of the distribution). Therefore, some researchers have proposed to consider the upper and lower bands for the dataset (Rao and Lakshmi 2005; Shiotani 2001). This method is referred to as the Improved b-value in the literature. If the b-values are calculated based on incremental intervals, the method is referred to as the incrementally improved b-value (Inc-Ib). The upper limit and lower limit are defined by A_2 and A_1

$$A_2 = \mu - \alpha_1\sigma \quad \text{and} \quad A_1 = \mu + \alpha_2\sigma \tag{4}$$

The slope between the upper and lower limits in the log N versus the amplitude distribution results in an improved b-value (Ib). This calculation is based on the assumption that the distribution between the upper and lower limits is linear

$$Ib = \frac{[\log A_1 - \log A_1]}{[A_2 - A_1]} \tag{5}$$

In this study, instead of using the preceding equation, the average (μ) and standard deviation (σ) of each data subset is calculated, and the data, which exceed $\mu + \alpha_2\sigma$ or are less than $\mu - \alpha_1\sigma$, are deleted. Then, b-values for the remaining data are calculated. The parameters α_1 and α_2 range from 0.5 to 2. In this paper, α_1 and α_2 are set equal to unity.

Results

In this section, the results for the signal entropy and damage indices are presented. Entropies were first calculated for the medium-scale specimens. Then, entropies were calculated for large-scale and small-scale specimens and compared to the results for the medium-scale specimens. Finally, AE-based damage indices were calculated for the medium-scale specimens.

Entropy for the Medium-Scale Specimens

Discrete voltage entropy was calculated for the medium-scale specimens. The results for the confined and unconfined specimen are presented in Fig. 5. In the data, there are some blanks without data in which the experiment was stopped for maintenance and to check the sensors.

As seen in Fig. 5, the range of entropy values is almost the same for both specimens. The solid black line shows the average entropy in 50-day intervals. The voltage entropies in each interval were averaged, and the temporal trend of the averaged entropies is presented as solid lines in Fig. 5. The average entropies are presented in the secondary vertical axis to show the trend of curves better. Generally, the variation of the average entropy for both specimens were minor. The average entropy in the confined specimen increased up to 200 days and then decreased, while in the unconfined specimen, it increased up to 150 days and then had a generally decreasing trend, despite some fluctuations. Fig. 6 shows the average entropy for the 50-day intervals when using different bin sizes. Although slight variations in entropy values with different bin sizes

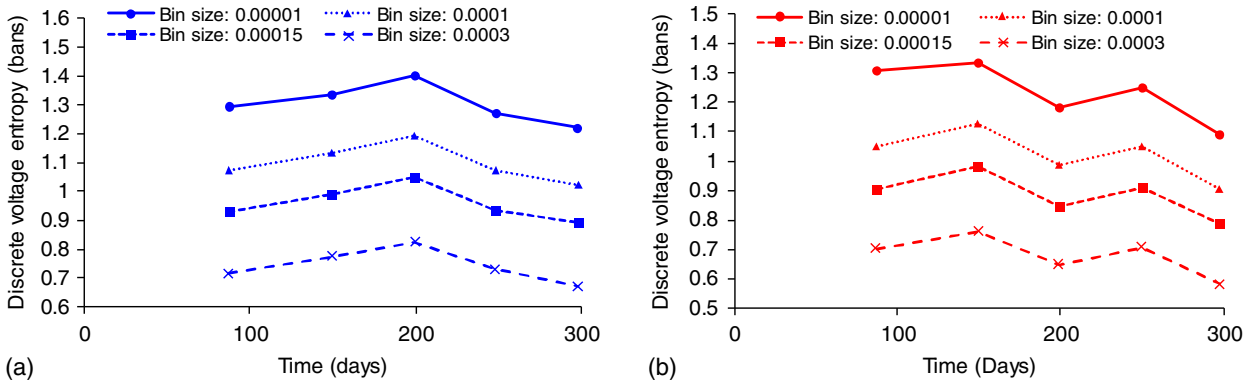

Fig. 6. Discrete voltage entropy for medium-scale specimens using different bin sizes: (a) confined; and (b) unconfined.

Pract. Period. Struct. Des. Constr., 2021, 26(1): 04020065

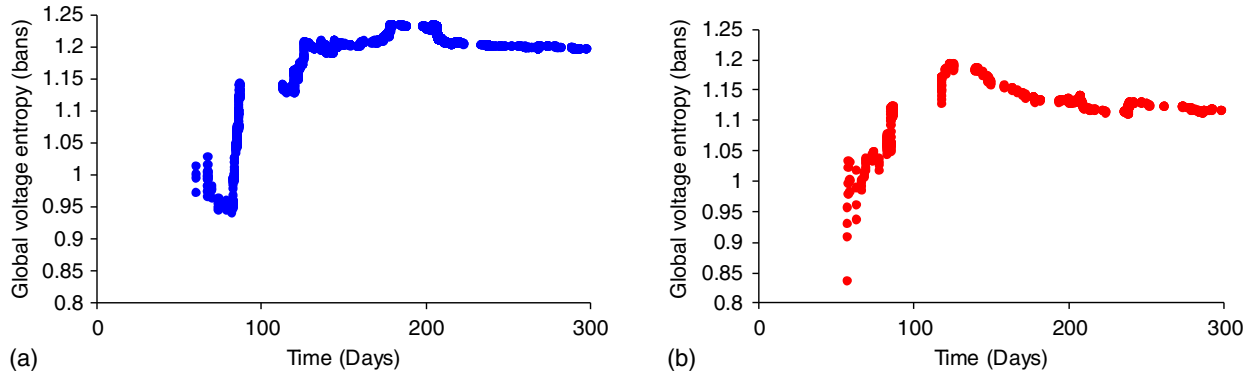

Fig. 7. Global voltage entropy (GVE) for medium-scale specimens: (a) confined; and (b) unconfined.

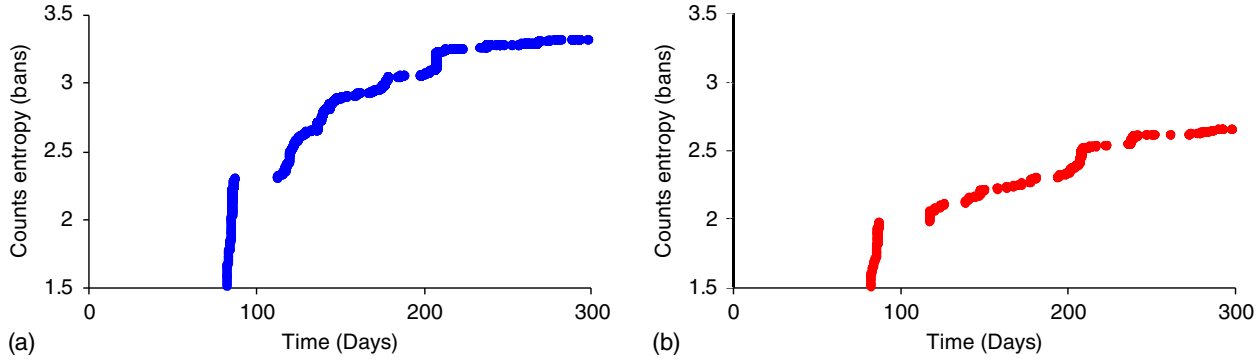

Fig. 8. Counts entropy (CE) for medium-scaled specimens: (a) confined; and (b) unconfined.

are observed, trends of entropy values with different bin sizes are similar, showing the trends of voltage entropies to be insensitive to the bin size.

The global voltage entropy was calculated for each desired time by considering all previously recorded data from the beginning of the test. The results for the bin size of the 0.0001 V are shown in Fig. 7. In the confined specimen, the GVE increased up to 200 days, and then it remained almost constant. In the unconfined specimen, the GVE increased up to 123 days and decreased slightly after that. The GVE remained almost constant after 180 days in the unconfined specimen. The trends of GVE in both specimens were similar to the patterns observed in DVE curves. At first, the entropy had an increasing trend and then a decreasing trend. Furthermore, the GVE range for the two specimens was similar, although the peak value for the confined specimen was slightly larger than the unconfined specimen.

The second entropy method is to calculate the entropy of counts, namely, the counts-entropy. Two different approaches were utilized in this paper for calculating the probability distribution. The results for the first method (as mentioned in the section "Signal Entropy") are illustrated in Fig. 8. As seen in the figure, the CE rates were much higher earlier in the experiment rather than later. The CE rates for both specimens declined by the specimen age. The CE variation in the confined specimen was almost constant after 200 days, while the CE variation in the unconfined specimen was constant after 237 days. The CE values for the confined specimen were more than for the unconfined specimens. The reason might be related to the dependency of this method on the number of signals, which were larger for the confined specimen.

The second method utilized for calculating the counts-entropy was by deriving the empirical CDF and PDF of the counts; the results are presented in Fig. 9. The values for CE_CDF for both specimens were almost in the same range, contrary to the CE values (Fig. 8). Therefore, it can be concluded that the CE_CDF did not depend on the number of hits contrary to the CE.

The CE_CDF values for both specimens had an increasing trend and reached a peak value, followed by a decreasing trend. In the unconfined specimen, the decreasing trend started earlier than for the confined specimen, although there was a slight increase at 242 days for the unconfined specimen.

Voltage Entropies for Specimens with Different Scales

In this section, the voltage entropies for the three types of specimens: large-scale, medium-scale, and small-scale, are discussed. The compressive load was applied on a cement paste prism (small-scale specimen) and stopped when the load reached 40% of the expected ultimate capacity. The DVE was calculated for each signal by using a bin size of 0.0001 V; the results are presented in Fig. 10(a). The entropy ranged from 0.69 to 2.6.

The cumulative voltage entropy and CSS are presented in Fig. 10(b). The trend of the cumulative entropy was different from the CSS for the small-scale specimen, despite a correlation between two parameters. The difference was clearer before the jump in the CSS at the end of loading. The correlation coefficient between the CSS and the cumulative entropy is 0.907. The cumulative entropy increased with a constant rate and then experienced a sudden jump at the end of loading. The cumulative entropy showed two phases

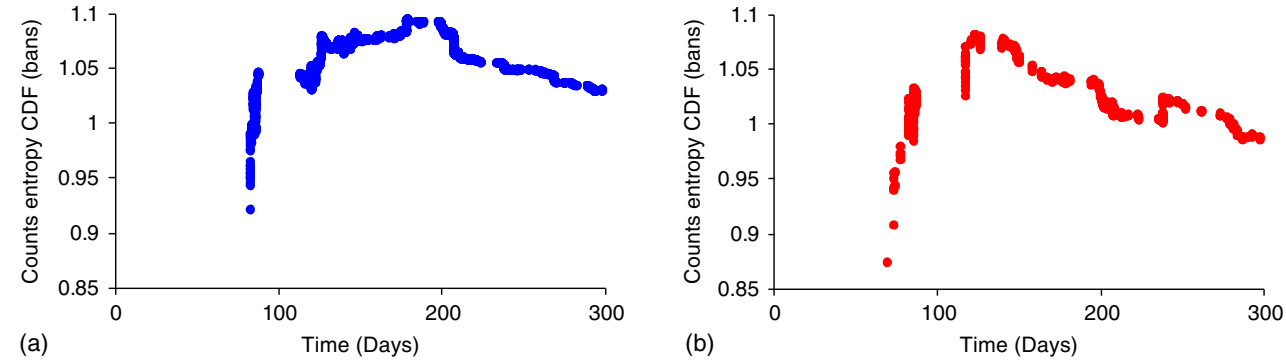

Fig. 9. Counts entropy using CDF (CE_CDF) for medium-scale specimens: (a) confined; and (b) unconfined.

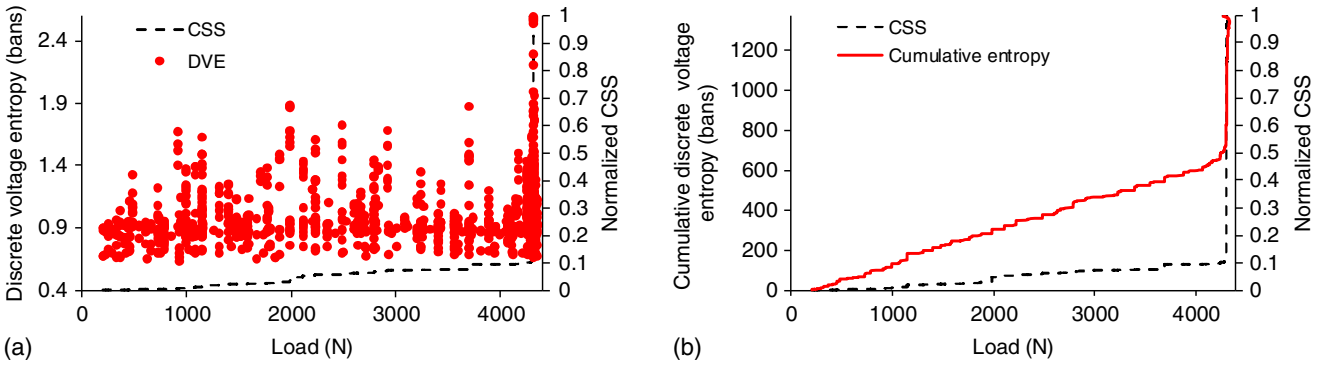

Fig. 10. Discrete voltage entropy (DVE) and cumulative entropy for small-scale specimens: (a) discrete voltage entropy; and (b) cumulative entropy.

of cracking in the cement paste. The first phase is potentially related to the microcrack formation, and the second phase, at the end of loading, is more likely associated with an unstable crack formation, propagation, and coalescence of existing cracks and formation of macrocracks (Anay et al. 2018).

Voltage entropies for the medium-scale and large-scale specimens are presented in Figs. 11 and 12, respectively. The DVE values for the medium-scale confined specimen ranged between 0.42 to 2.57, and the DVE values for the medium-scale unconfined specimen ranges were between 0.4 and 2.03. The correlation between the CSS and cumulative entropy for the medium-scale and large-scale specimens is higher than the correlation for the small-scale specimen, as seen in Figs. 11 and 12, which might be due to the differences in the loading and boundary conditions for the specimens under ASR versus compressive loading. The correlation coefficients between the CSS and cumulative entropy for the medium-scale confined and unconfined specimen are 0.996. The correlation coefficients for the large-scale confined and unconfined specimens are 0.999 and 0.995, respectively.

The entropy values for the large-scale confined specimen (Fig. 12) ranged from 0.5 to 1.4, and the entropy for the large-scale unconfined specimen ranged from 0.46 to 1.5.

The distributions of voltage entropies for all specimens were estimated using nonparametric kernel distribution (Wand and Jones 1994; Epanechnikov 1969) and are presented in Fig. 13. In addition, the PDF of the signal strength is also illustrated in Fig. 13(b) for comparison. The variation of the voltage entropies for all specimens is much less than the variation of the signal strength, indicating the dimensional independence of the entropy.

The ranges of voltage entropies for the specimens with different scales are similar. Therefore, the Shannon entropy can be contemplated as a parameter that may be used to compare AE data for specimens with different scales but similar boundary conditions and sensor type. The differences in the entropy trends between the specimens were due to different materials, boundary conditions, loading conditions, number of sensors, and sensor types. The specimens in this study were made of different materials. The small-scale specimen was a cement paste prism. The confined and unconfined medium-scale specimens were reinforced concrete and plain concrete, respectively. The large-scale specimens were also reinforced concrete. The cement paste material is more brittle and more homogeneous than concrete. Consequently, the cracking mechanism of the small-scale specimen was different from the medium-scale and large-scale specimens. The wave scattering at the beginning of loading in the small-scale specimen was expected to be less than other specimens because the small-scale specimen did not contain aggregate or reinforcement. The loading condition was also reflected in the inconsistencies between the entropy trends. The cement-paste was under compressive load, while no external loading was applied on the medium-scale and large-scale specimens. The medium-scale and large-scale specimens were exposed to the ASR expansion, and the expansion resulted in internal strains. The ASR-induced stresses were gradually formed in the specimens, while the external loading on the cement paste was applied within a much shorter time compared to the ASR process. The number of sensors and sensor coupling also were other important factors that may influence the entropy trends. In the large-scale specimens, only three broadband sensors were used to monitor a large volume of concrete, while in the medium-scale specimens, a much denser sensor layout per volume of concrete (ten sensors) was employed. The attachment of the sensors was another potentially important factor. In the large-scale specimens, the sensors were embedded inside the specimens

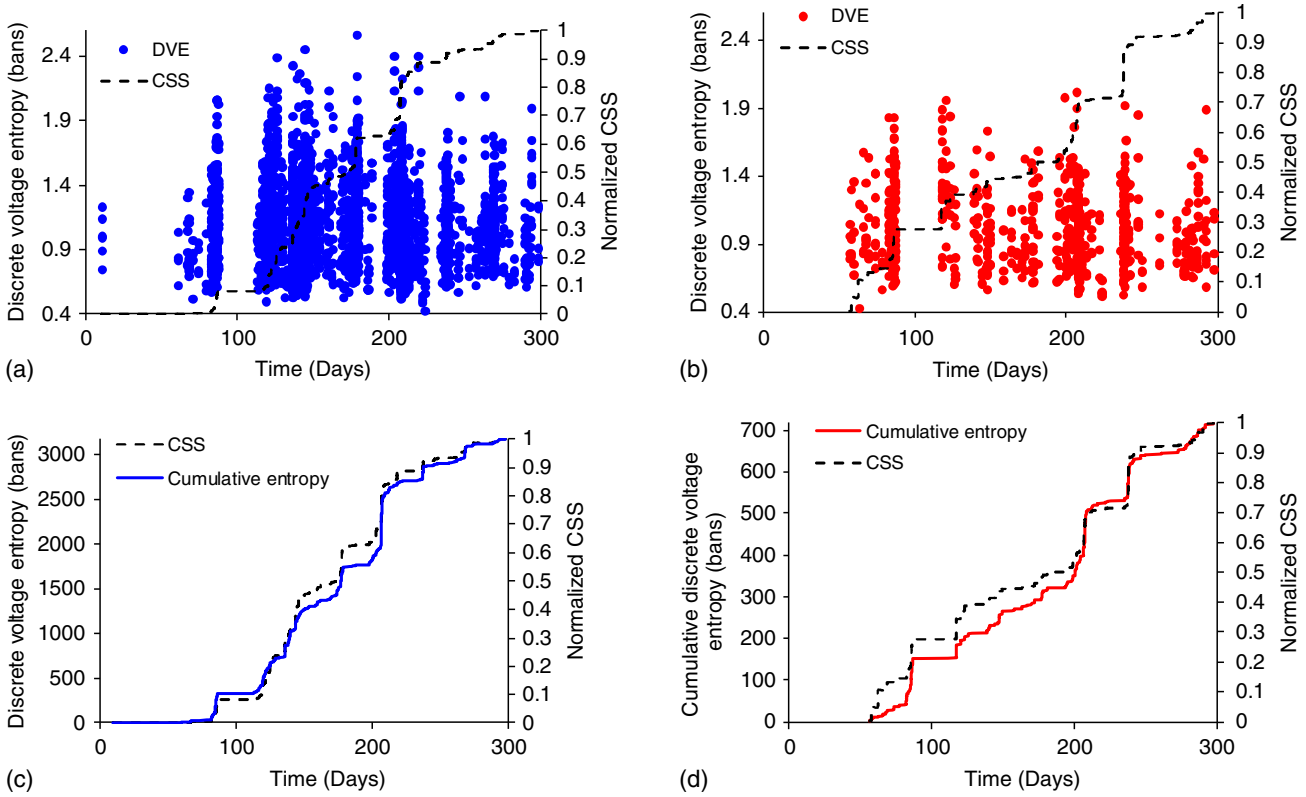

Fig. 11. Discrete voltage entropy and cumulative entropy for medium-scale specimens: (a) discrete voltage entropy for the confined specimen; (b) discrete voltage entropy for the unconfined specimen; (c) cumulative entropy for the confined specimen; and (d) cumulative entropy for the unconfined specimen.

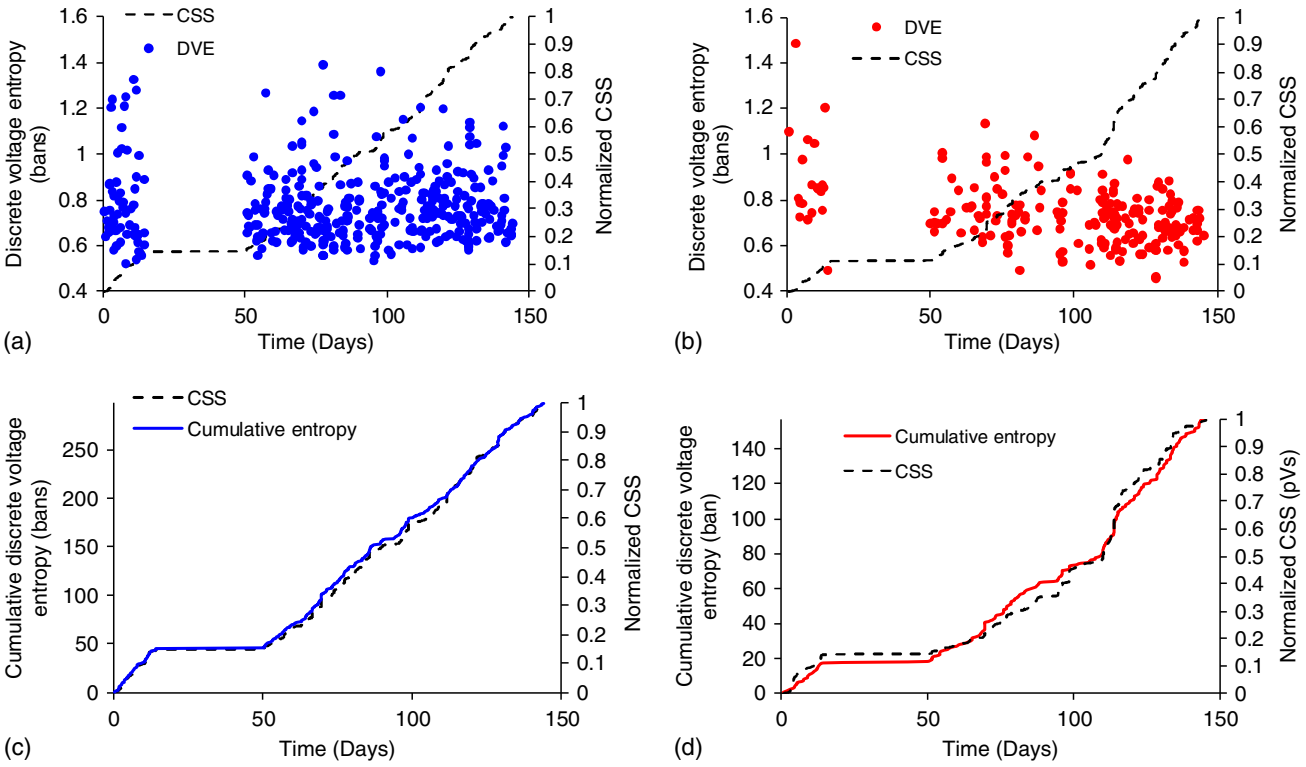

Fig. 12. Discrete voltage entropy and cumulative entropy for large-scale specimens: (a) discrete voltage entropy for the confined specimen; (b) discrete voltage entropy for the unconfined specimen; (c) cumulative entropy for the confined specimen; and (d) cumulative entropy for the unconfined specimen.

Pract. Period. Struct. Des. Constr., 2021, 26(1): 04020065

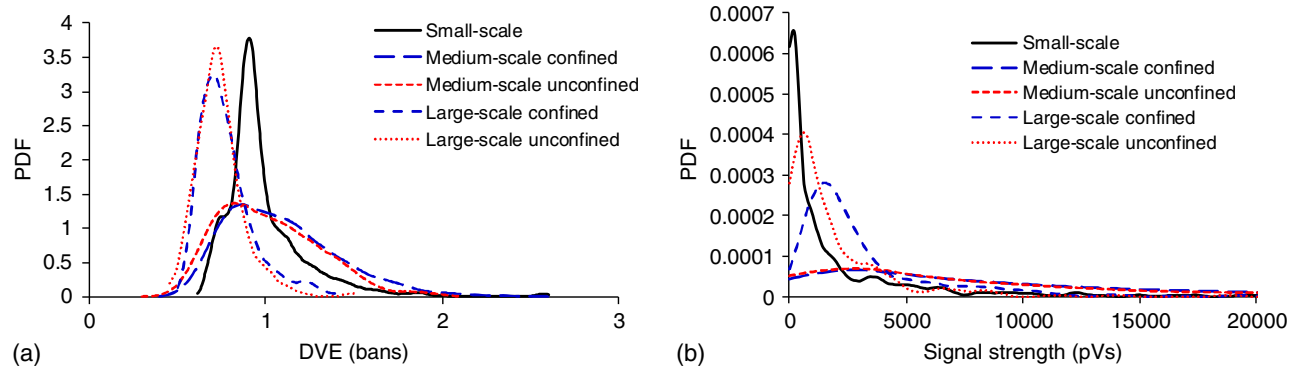

Fig. 13. Probability distribution functions of signal strength and entropy: (a) distribution of voltage entropy; and (b) distribution of signal strength.

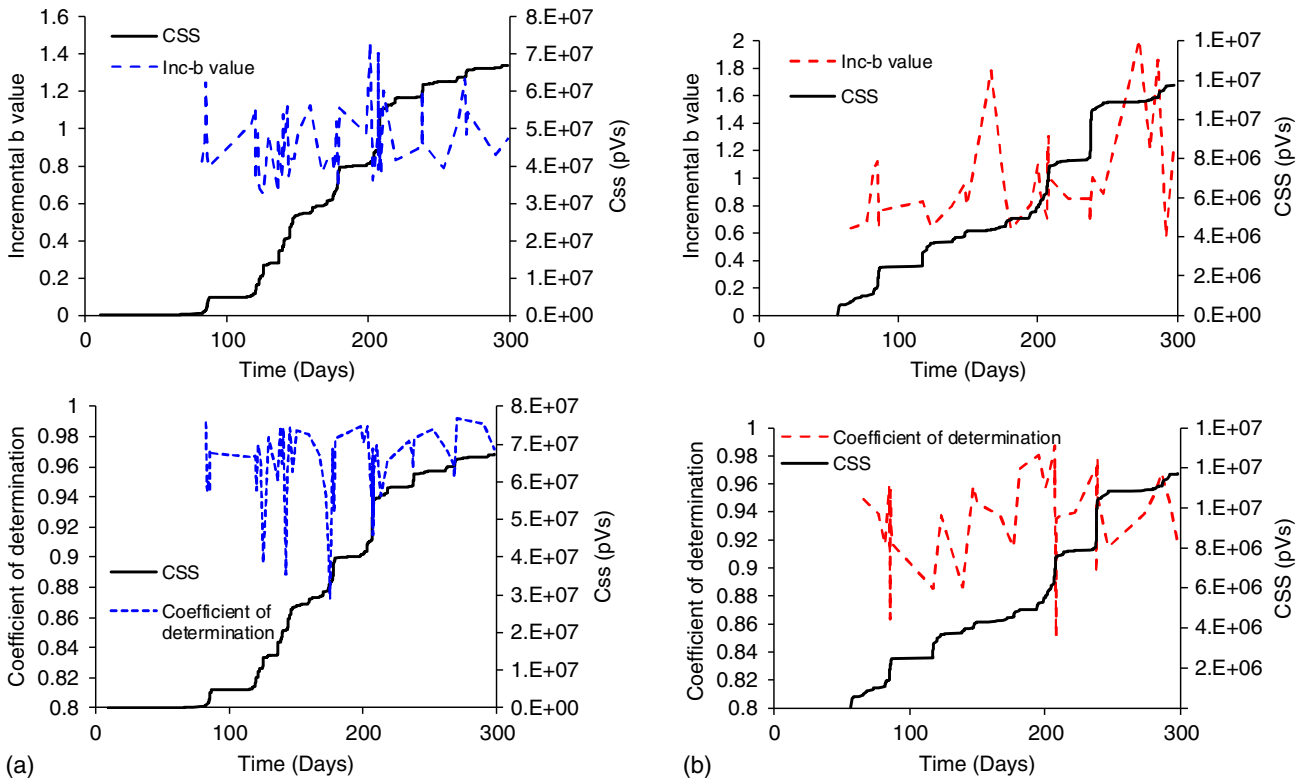

Fig. 14. Incremental *b*-values and coefficients of determination of amplitude distribution for medium-scale specimens: (a) confined specimen; and (b) unconfined specimen.

before casting. The concrete shrinkage may reduce the contact between the sensor and concrete. However, in the medium-scale specimens, the sensors were attached to the specimen surfaces using epoxy, and constant pressure was applied to the sensors by the holders (Soltangharaei et al. 2018b). In the small-scale specimen, the sensors were also affixed on the surfaces, using epoxy and hot glue. The sensor types may also influence the entropy trends. The operating frequency range and sensitivity of the sensors utilized for three specimen types were different.

b-Value Analysis

The Inc-*b* values and coefficients of determination of the amplitude distributions were calculated for the medium-scale specimens (confined and unconfined), and the results are shown in Fig. 14. The *b*-values did not have a clear correlation with the CSS in either specimen. However, the coefficients of determination illustrated a clear correlation with the CSS. The coefficients of determination abruptly decreased at the jumps in the CSS curve. In the confined specimen, the sudden drops in the coefficients of determination occurred at 174 and 207 days when the large CSS jumps happened. In addition, in the unconfined specimen, a similar correlation was observed. For instance, the coefficients of determination decreased at 207 and 237 days. When severe damage happened in the specimens, a large amount of acoustic energy was expected to be released, which would generate AE data with strong signal strength and amplitude. The signals that generated a large amount of energy acted as outliers for the amplitude-log *N* distribution and made the

Pract. Period. Struct. Des. Constr., 2021, 26(1): 04020065

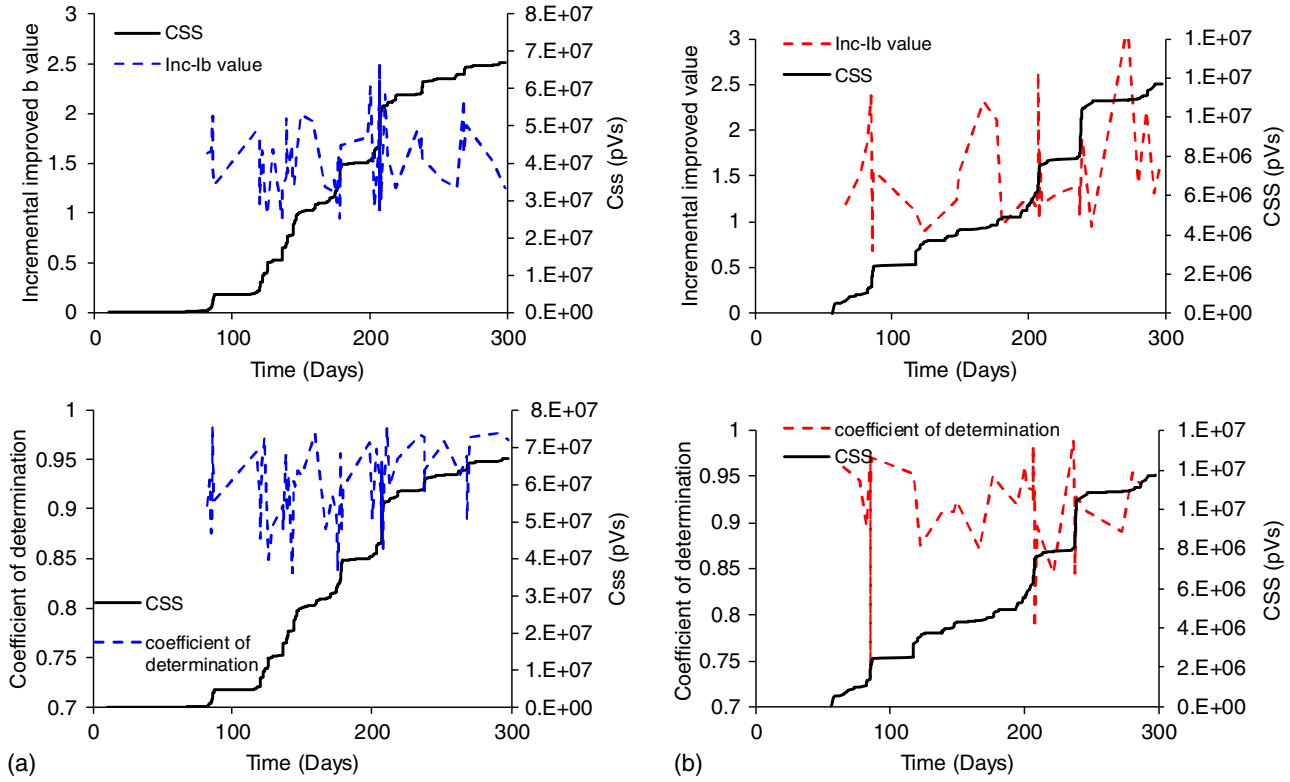

Fig. 15. Incremental improved *b*-values and coefficients of determination of amplitude distribution for medium-scale specimens: (a) confined specimen; and (b) unconfined specimen.

distribution deviate more from linearity. This deviation resulted in a lower coefficient of determination.

The incrementally improved *b*-values were also calculated by deleting the data, which were outside of the average plus/minus standard deviation ($\mu \pm \sigma$) in each interval. The results are illustrated in Fig. 15. The slight reductions in the Inc-*Ib* values were observed at the jumps in the CSS curve. The sudden reductions in the coefficients of determination were more apparent than the Inc-*Ib* values.

From the preceding observations, it is concluded that *b*-values did not show clear temporal trends for the specimens under the ASR-induced expansion. On the other hand, the coefficient of determination can be used as an indicator to detect the occurrence of significant damage in lieu of the *b*-value.

Conclusion

In this study, information entropy was calculated using different methods for the AE data recorded during the ASR process, and comparisons have been made between different methods. The efficacy of entropy for damage detection of concrete structures affected by ASR was evaluated in addition to studying the temporal evolution of entropies in the specimens. Moreover, an application of intensity, *b*-value analysis, and CSS gradient was evaluated for the concrete specimens affected by the ASR without external loading. The following are the conclusions drawn from the study:

- Although there were only minor variations in the discrete voltage entropy values, a trend was observed in the average values of the entropy in terms of the experiment time. The average entropy values initially showed an increasing trend, followed by a decreasing trend. The decreasing trend started earlier for the unconfined medium-scale specimen than the confined specimen. A similar trend was also observed in the global voltage entropy and counts-entropy using CDF for the medium-scale specimens. The entropy initially increased and then decreased or stayed constant at the later stages of ASR (after 200 days and 150 days for the confined and unconfined specimens). The information entropy quantifies the randomness of events. In this context, the randomness of events initially increased in the specimens and later decreased. At the earlier ASR stage, the microcracks randomly occurred inside the specimens. The random microcrack formations were reflected in the increasing entropy values. As the ASR progressed, the macrocracks formed in specific locations with a larger stress concentration and less strength. Therefore, the occurrence of macrocracks was less randomized. Therefore, entropy had a decreasing trend at this stage.
- The variations of the *b*-values in terms of time for the confined and unconfined specimens were almost constant, and the *b*-values did not show any obvious temporal trend. However, a correlation was observed between the coefficient of determination and the CSS curves. The coefficients of determination dropped as the CSS jumps, which indicates that the coefficients of determination were more sensitive to the damage formation than *b*-values. The coefficients of determination were dropped to less than 92% at the large jumps in the CSS curves. The use of coefficients of determination is recommended for the ASR damage identification in time.
- Comparing the discrete voltage entropies for different specimens, it was observed that entropy ranges were not significantly changed by the specimen scale, boundary and loading conditions, and specimen types. Therefore, this parameter may hold promise as an alternative for the comparison of the damage conditions between different structures in terms of AE data.

Pract. Period. Struct. Des. Constr., 2021, 26(1): 04020065

Data Availability Statement

Data and models generated or used during the study are available from the corresponding author by request.

Acknowledgments

This research was partially supported by the US Department of Energy—Nuclear Energy University Program (NEUP) under the contract DE-NE0008544 and the US Department of Energy Office of Science, Office of Basic Energy Sciences, and Office of Biological and Environmental Research under Award No. DE-SC-00012530.

References

Abdelrahman, M., M. K. ElBatanouny, and P. H. Ziehl. 2014. "Acoustic emission based damage assessment method for prestressed concrete structures: Modified index of damage." *Eng. Struct.* 60 (Feb): 258–264. https://doi.org/10.1016/j.engstruct.2013.12.037.

Abdelrahman, M., M. K. ElBatanouny, P. H. Ziehl, J. Fasl, C. J. Larosche, and J. Fraczek. 2015. "Classification of alkali–silica reaction damage using acoustic emission: A proof-of-concept study." *Constr. Build. Mater.* 95 (Oct): 406–413. https://doi.org/10.1016/j.conbuildmat.2015.07.093.

Allard, A., S. Bilodeau, F. Pissot, B. Fournier, J. Bastien, and B. Bissonnette. 2018. "Expansive behavior of thick concrete slabs affected by alkali-silica reaction (ASR)." *Constr. Build. Mater.* 171 (May): 421–436. https://doi.org/10.1016/j.conbuildmat.2018.03.159.

Amiri, M., and M. Modarres. 2014. "An entropy-based damage characterization." *Entropy* 16 (12): 6434–6463. https://doi.org/10.3390/e16126434.

Amiri, M., M. Modarres, and E. L. Droguett. 2015. "AE entropy for detection of fatigue crack initiation and growth." In *Proc., 2015 IEEE Conf. on Prognostics and Health Management*, 1–8. New York: IEEE.

Anay, R., V. Soltangharaei, L. Assi, T. DeVol, and P. Ziehl. 2018. "Identification of damage mechanisms in cement paste based on acoustic emission." *Constr. Build. Mater.* 164 (Mar): 286–296. https://doi.org/10.1016/j.conbuildmat.2017.12.207.

Bach, F., T. S. Thorsen, and M. Nielsen. 1993. "Load-carrying capacity of structural members subjected to alkali-silica reactions." *Constr. Build. Mater.* 7 (2): 109–115. https://doi.org/10.1016/0950-0618(93)90040-J.

Barbosa, R. A., S. G. Hansen, K. K. Hansen, L. C. Hoang, and B. Grelk. 2018. "Influence of alkali-silica reaction and crack orientation on the uniaxial compressive strength of concrete cores from slab bridges." *Constr. Build. Mater.* 176 (Jul): 440–451. https://doi.org/10.1016/j.conbuildmat.2018.03.096.

Chai, M., Z. Zhang, and Q. Duan. 2018. "A new qualitative acoustic emission parameter based on Shannon's entropy for damage monitoring." *Mech. Syst. Sig. Process.* 100 (Feb): 617–629. https://doi.org/10.1016/j.ymssp.2017.08.007.

Clark, L. 1989. *Critical review of the structural implications of the alkali silica reaction in concrete*. Crowthone, UK: Transportation and Road Research Laboratory.

Colombo, I. S., I. Main, and M. Forde. 2003. "Assessing damage of reinforced concrete beam using '*b*-value' analysis of acoustic emission signals." *J. Mater. Civ. Eng.* 15 (3): 280–286. https://doi.org/10.1061/(ASCE)0899-1561(2003)15:3(280).

Epanechnikov, V. A. 1969. "Non-parametric estimation of a multivariate probability density." *Theory Probab. Appl.* 14 (1): 153–158. https://doi.org/10.1137/1114019.

Farnam, Y., M. R. Geiker, D. Bentz, and J. Weiss. 2015. "Acoustic emission waveform characterization of crack origin and mode in fractured and ASR damaged concrete." *Cem. Concr. Compos.* 60 (Jul): 135–145. https://doi.org/10.1016/j.cemconcomp.2015.04.008.

Fernandes, I., and M. Broekmans. 2013. "Alkali–silica reactions: An overview. Part I." *Metall. Microstruct. Anal.* 2 (4): 257–267. https://doi.org/10.1007/s13632-013-0085-5.

Fournier, B., M.-A. Berube, K. J. Folliard, and M. Thomas. 2010. *Report on the diagnosis, prognosis, and mitigation of alkali-silica reaction (ASR) in transportation structures*. Rep. No. FHWA-HIF-09-004. Washington, DC: Federal Highway Administration.

Garcia-Diaz, E., J. Riche, D. Bulteel, and C. Vernet. 2006. "Mechanism of damage for the alkali–silica reaction." *Cem. Concr. Res.* 36 (2): 395–400. https://doi.org/10.1016/j.cemconres.2005.06.003.

Hayes, N. W., Q. Gui, A. Abd-Elssamd, Y. Le Pape, A. B. Giorla, S. Le Pape, E. R. Giannini, and Z. J. Ma. 2018. "Monitoring alkali-silica reaction significance in nuclear concrete structural members." *J. Adv. Concr. Technol.* 16 (4): 179–190. https://doi.org/10.3151/jact.16.179.

Islam, M. S., and N. Ghafoori. 2018. "A new approach to evaluate alkali-silica reactivity using loss in concrete stiffness." *Constr. Build. Mater.* 167 (Apr): 578–586. https://doi.org/10.1016/j.conbuildmat.2018.02.047.

Jung, D. Y., Y. Mizutani, A. Todoroki, and Y. Suzuki. 2017. "Frequency dependence of the *b*-value used for acoustic emission analysis of glass fiber reinforced plastics." *Open J. Compos. Mater.* 7 (3): 117. https://doi.org/10.4236/ojcm.2017.73007.

Kahirdeh, A. 2014. "Energy dissipation and entropy generation during the fatigue degradation: Application to health monitoring of composites." LSU Doctoral dissertations, Dept. of Mechanical and Industrial Engineering, Louisiana State Univ.

Kahirdeh, A., and M. Khonsari. 2016. "Acoustic entropy of the materials in the course of degradation." *Entropy* 18 (8): 280. https://doi.org/10.3390/e18080280.

Kahirdeh, A., C. Sauerbrunn, and M. Modarres. 2017a. "Acoustic emission entropy as a measure of damage in materials." In *Proc., AIP Conf.*, 060007. Melville, NY: American Institute of Physics.

Kahirdeh, A., C. Sauerbrunn, H. Yun, and M. Modarres. 2017b. "A parametric approach to acoustic entropy estimation for assessment of fatigue damage." *Int. J. Fatigue* 100 (Jul): 229–237. https://doi.org/10.1016/j.ijfatigue.2017.03.019.

Lamonaca, F., A. Carrozzini, D. Grimaldi, and R. S. Olivito. 2014. "Improved accuracy of damage index evaluation in concrete structures by simultaneous hardware triggering." *Metrol. Meas. Syst.* 21 (2): 341–350. https://doi.org/10.2478/mms-2014-0029.

Lokajíček, T., R. Přikryl, Š. Šachlová, and A. Kuchařová. 2017. "Acoustic emission monitoring of crack formation during alkali silica reactivity accelerated mortar bar test." *Eng. Geol.* 220 (Mar): 175–182. https://doi.org/10.1016/j.enggeo.2017.02.009.

Nair, A., and C. Cai. 2010. "Acoustic emission monitoring of bridges: Review and case studies." *Eng. Struct.* 32 (6): 1704–1714. https://doi.org/10.1016/j.engstruct.2010.02.020.

Noorsuhada, M. 2016. "An overview on fatigue damage assessment of reinforced concrete structures with the aid of acoustic emission technique." *Constr. Build. Mater.* 112 (Jun): 424–439. https://doi.org/10.1016/j.conbuildmat.2016.02.206.

Rajabipour, F., E. Giannini, C. Dunant, J. H. Ideker, and M. D. Thomas. 2015. "Alkali–silica reaction: Current understanding of the reaction mechanisms and the knowledge gaps." *Cem. Concr. Res.* 76 (Oct): 130–146. https://doi.org/10.1016/j.cemconres.2015.05.024.

Rao, M., and K. P. Lakshmi. 2005. "Analysis of b-value and improved b-value of acoustic emissions accompanying rock fracture." *Curr. Sci.* 89 (9): 1577–1582.

Sagasta, F., M. E. Zitto, R. Piotrkowski, A. Benavent-Climent, E. Suarez, and A. Gallego. 2018. "Acoustic emission energy *b*-value for local damage evaluation in reinforced concrete structures subjected to seismic loadings." *Mech. Syst. Sig. Process.* 102 (Mar): 262–277. https://doi.org/10.1016/j.ymssp.2017.09.022.

Saouma, V. E., and M. A. Hariri-Ardebili. 2014. "A proposed aging management program for alkali silica reactions in a nuclear power plant." *Nucl. Eng. Des.* 277 (Oct): 248–264. https://doi.org/10.1016/j.nucengdes.2014.06.012.

Sauerbrunn, C. M. 2016. "Evaluation of information entropy from acoustic emission waveforms as a fatigue damage metric for Al7075-T6." Ph.D. dissertation, Dept. of Mechanical Engineering, Univ. of Maryland.

Shiotani, T. 2001. "Application of the AE improved b-value to quantitative evaluation of fracture process in concrete-materials." *J. Acoust. Emiss.* 19 (Jan–Dec): 118–133.

Sinno, N., and M. H. Shehata. 2019. "Effect of sample geometry and aggregate type on expansion due to alkali-silica reaction." *Constr. Build. Mater.* 209 (Jun): 738–747. https://doi.org/10.1016/j.conbuildmat.2019.03.103.

Soltangharaei, V., R. Anay, L. Ai, E. R. Giannini, J. Zhu, and P. Ziehl. 2020. "Temporal evaluation of ASR cracking in concrete specimens using acoustic emission." *J. Mater. Civ. Eng.* 32 (10): 04020285. https://doi.org/10.1061/(ASCE)MT.1943-5533.0003353.

Soltangharaei, V., R. Anay, L. Assi, P. Ziehl, and F. Matta. 2018a. "Damage identification in cement paste amended with carbon nanotubes." In *Proc., AIP Conf.*, 030006. Melville, NY: American Institute of Physics.

Soltangharaei, V., R. Anay, N. Hayes, L. Assi, Y. Le Pape, Z. Ma, and P. Ziehl. 2018b. "Damage mechanism evaluation of large-scale concrete structures affected by alkali-silica reaction using acoustic emission." *Appl. Sci.* 8 (11): 2148. https://doi.org/10.3390/app8112148.

Thomas, M. D. A., K. J. Folliard, B. Fournier, P. Rivard, T. Drimalas, and S. I. Garber. 2013. *Methods for evaluating and treating ASR-affected structures: Results of field application and demonstration projects—Volume II: Details of field applications and analysis.* Rep. No. FHWA-HIF-14-0003. Washington, DC: Federal Highway Administration, USDOT.

Unnthorsson, R., T. P. Runarsson, and M. T. Jonsson. 2008. "AE entropy for the condition monitoring of CFRP subjected to cyclic fatigue." *J. Acoust. Emiss.* 26 (Jan–Dec): 262–269.

Wand, M. P., and M. C. Jones. 1994. *Kernel smoothing*. Boca Raton, FL: Chapman and Hall.

Zhang, X., N. Feng, Y. Wang, and Y. Shen. 2015. "Acoustic emission detection of rail defect based on wavelet transform and Shannon entropy." *J. Sound Vib.* 339 (Mar): 419–432. https://doi.org/10.1016/j.jsv.2014.11.021.